Geophysical Journal International

Geophys. J. Int. (2022) **230,** 70–83
Advance Access publication 2022 February 08
GJI Seismology

https://doi.org/10.1093/gji/ggac048

Recovery of Love wave overtone waveforms and dispersion curves from single-station seismograms using time-warping

M.G. Brown,[1] G. Lin,[1] H. Matsuzawa[2,*] and K. Yoshizawa[2,3]

[1]*Rosenstiel School of Marine and Atmospheric Sciences, University of Miami,* 4600 *Rickenbacker Cswy., Miami, FL* 33149*, USA. E-mail: mbrown@rsmas.miami.edu*
[2]*Department of Natural History Sciences, Graduate School of Science, Hokkaido University, Sapporo* 060-0810*, Japan*
[3]*Department of Earth and Planetary Sciences, Faculty of Science, Hokkaido University, Sapporo* 060-0810*, Japan*

Accepted 2022 February 4. Received 2022 January 31; in original form 2021 October 6

SUMMARY

Time-warping is a signal processing technique that, when applied to an isolated measurement of a transient signal that propagates in a waveguide, allows contributions to that signal from individual mode numbers to be isolated and extracted. Dispersion curves for individual mode numbers can, in turn, be recovered. Isolation of contributions associated with individual mode numbers is possible because after time-warping—a special environmentally dependent non-uniform sampling—is applied, the signal energy corresponding to each mode number is isolated in the frequency spectrum of the time-warped signal. Here we derive the time-warping transform for teleseismic Love waves, assuming the Earth structure is approximately known, and we illustrate the utility of time-warping using both synthetic and measured seismograms.

Key words: Time-series analysis; Guided waves; Surface waves and free oscillations.

1 INTRODUCTION

Teleseismic surface waves provide strong constraints on mantle structure and, in particular, anisotropy of the mantle. Love waves, the focus of this paper, play a critical role in this context as they are controlled by the lateral shear wave velocity. Love waves are naturally described as a superposition of normal modes, the toroidal modes in a spherical earth model. Love waves in the Earth are strongly dispersive. A useful, but challenging, approach to Love wave analysis is to try to recover from measured seismograms the waveforms associated with individual mode numbers and the corresponding dispersion curves. Overtone waveforms are particularly useful to constrain mantle structure in the lower portion of the upper mantle, within the transition zone and in the lower mantle. In typical measured seismograms some portion of the fundamental mode waveform is temporally isolated from overtone waveforms, while overtone waveforms overlap in time with each other and with the early low-frequency portion of the fundamental mode waveform. Under such conditions, the problem of isolating overtone waveforms is extremely challenging. Array processing techniques provide a robust means to address this problem. Previous use of these and other competing techniques are briefly reviewed below. Array-processing-based approaches are well suited to continental stations where a dense measurement array is present. In this paper we demonstrate that it is possible to apply a recently developed signal processing technique known as time-warping to a seismogram measured at an isolated location to extract fixed-mode-number waveforms and corresponding dispersion curves. We demonstrate the utility of time-warping in the analysis of Love waves using both synthetic and measured seismograms. Time-warping has some shortcomings, which we discuss. In spite of these shortcomings, the results presented here lead us to anticipate that time-warping will prove to be a useful Love wave analysis tool which is applicable in the challenging situation in which the only information available is a seismogram measured at an isolated location, for example at an island-based station.

Methods to extract fixed-mode-number waveforms for teleseismic Love waves, especially overtone waveforms, have been developed only recently, but the general problem of estimating surface wave (both Rayleigh and Love waves) dispersion curves from measured seismograms has deep roots. Following (Matsuzawa & Yoshizawa 2019), we break these analysis methods into three groups: single-station methods, interstation methods and array-based methods. The simplest single-station method is the frequency-time analysis (FTAN) introduced by Levshin *et al.* (1972), which has been used principally to estimate some portion of a temporally resolved fundamental mode dispersion curve. More complicated single-station methods are based on single-mode waveform fitting (Trampert & Woodhouse 1995; Ekström *et al.* 1997), mode stripping (van Heijst & Woodhouse 1997), and multimode waveform fitting (Yoshizawa & Kennett 2002; Visser *et al.* 2007; Yoshizawa & Ekström 2010). A disadvantage of these methods is that they require calculation of synthetic seismograms, which in turn requires knowledge of the source function. Interstation methods (Dziewonski &

*Now at: Sapporo Regional Headquarters, Japan Meteorological Agency, Sapporo 060-0002, Japan.

Hales 1972; Forsyth & Li 2005; Pedersen 2006; Lin *et al.* 2009; Lin & Ritzwoller 2011; Foster *et al.* 2014a, b; Hamada & Yoshizawa 2015) make use of phase differences between seismograms measured at different stations to estimate phase speeds. Linear-array-based methods (Nolet 1975, 1976; Luo *et al.* 2015) involve analysis of multiple stations that lie approximately on a common great circle path; such an array allows one to perform an f–k (frequency and local lateral wavenumber) decomposition of the measured seismograms. Most recently (Matsuzawa & Yoshizawa 2019) have combined traditional linear array analysis methods with the use of the linear Radon transform (Luo *et al.* 2008, 2009, 2015) and have shown that this combination of analysis methods is capable of isolating fixed mode number waveforms for both Love and Rayleigh waves under conditions in which the extracted waveforms overlap in time.

In this paper, we make use of a signal processing technique known as time warping. In spite of its less-than-serious sounding name, time-warping rests on a firm mathematical foundation. Time-warping is one of a larger class of unitary similarity transformations (Baraniuk & Jones 1995); such transformations preserve energy and inner products. Applicability of time-warping to signals propagating in a waveguide was established by Le Touzé *et al.* (2009). Specifically, in that paper the time-warping transform was derived for sound waves propagating in a particular waveguide, and it was shown that application of that transform allows one to isolate non-temporarily resolved fixed-mode-number contributions to a propagating transient signal. The waveguide considered in that paper, sometimes referred to as the ideal shallow water waveguide, consists of a homogeneous fluid (ocean) with a flat rigid bottom and a pressure-release surface. The ideal shallow water waveguide is sometimes used as an approximate model of coastal underwater acoustic environments; not surprisingly, then, availability of the time-warping transform for this environment stimulated a number of publications involving application of that transform (Bonnel *et al.* 2010, 2011, 2013, 2020; Bonnel & Chapman 2011; Zeng *et al.* 2013; Brown *et al.* 2016; Duan *et al.* 2016; Sergeev *et al.* 2017; Godin *et al.* 2019; Tan *et al.* 2019). These papers reveal that, although the time-warping transform depends on the environment in which it is applied, the procedure is robust in the sense that the environment used to derive the transform need not accurately match the environment in which measurements are made. More recently, a general environmentally dependent time-warping transform was derived (Brown 2019) which reduces to the ideal shallow water waveguide time-warping transform as a special case. That general time-warping transform is the transform that is applied in the present paper. The ideal shallow water waveguide warping transform has the convenient property that the relationship between warped time t' and unwraped time t is specified analytically and is invertible so both $t'(t)$ and $t(t')$ have simple analytical forms. More generally, the transformations between t and t' are performed by making use of a table look-up procedure; this and related topics are discussed in more detail below.

We now provide a heuristic explanation of the basic principles underlying time-warping. The upper panel of Fig. 1 shows a set of dispersion curves in an idealized waveguide. This figure was motivated by Love waves in the Earth, but should not be thought of as representative of a realistic earth model. Here and below we label mode numbers starting with $m = 0$, the fundamental mode; $m = 1$ is the first overtone, etc. The coordinate axes used to plot dispersion curves in Fig. 1 and elsewhere in this paper are frequency f, the vertical axis, and group slowness S_g, the horizontal axis. This is done because the group slowness is a scaled time axis, $t = XS_g$, where X is epicentral distance, so the dispersion diagram is a time-frequency plot. A seismogram in the environment corresponding to the dispersion curves shown in the upper panel consists of a superposition—a sum over contributions from many mode numbers—of many FM (frequency modulated) sweeps. An example of one such FM sweep, corresponding to $m = 2$ at $X = 10\,000$ km, is shown in the middle panel. Note the correspondence between the local frequency of the FM sweep in the middle panel and the corresponding frequency for the $m = 2$ dispersion curve shown in the upper panel. Now imagine sampling the FM sweep in the middle panel with a variable sampling rate chosen so that there are exactly eight, say, samples per local period of the waveform. This non-uniform sampling is referred to as time-warping. If we then compute the Fourier spectrum of the

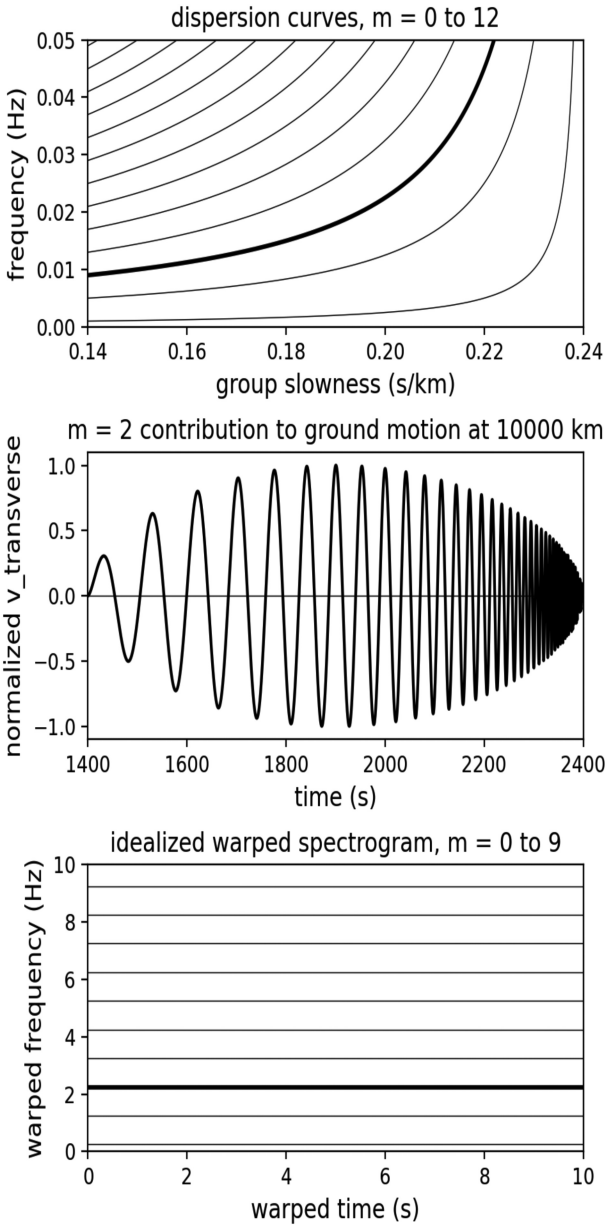

Figure 1. Illustration of time-warping. Upper panel: dispersion curves in an idealized environment. The heavy line corresponds to $m = 2$. Middle panel: The $m = 2$ waveform corresponding to the upper panel at epicentral distance $X = 10\,000$ km. Lower panel: idealized spectrogram of a multimode time-warped seismogram corresponding to the dispersion curves shown in the upper panel. The heavy line corresponds to $m = 2$.

time-warped signal (treating the sampling interval as if it were uniform) we would observe a line spectrum. This situation is illustrated in the lower panel of Fig. 1 as an idealized spectrogram, rather than a simple spectrum. The scaling of the warped frequency axis in that plot will be discussed below. The remarkable (and not obvious based on the meager description that we have given here) property of the time-warping transformation described below is that the same non-uniform sampling, that is the same time-warping transform, works for all mode numbers provided the asymptotic arguments described below hold. A consequence of the fact that the same time-warping transform works for all mode numbers is that, after applying that transform, the Fourier spectrum of a seismogram with contributions from many mode numbers will consist of many lines, with each spectral line corresponding to a different mode number. Details are provided below. The horizontal axes in the upper two panels of Fig. 1 are the same, with $t = XS_g$, but the horizontal axis in the lower panel is arbitrary because warped time approaches infinity as S_g approaches 0.24 s km^{-1} in the assumed environment. Because the spectral peaks in the warped frequency domain are isolated, with each peak corresponding to a distinct mode number, one need only apply a bandpass filter to the time-warped seismogram (in the time-warped domain) to isolate a fixed-m contribution to the original multimode seismogram. An inverse time-warping transform is then applied to eliminate the warping-induced temporal distortion of the single-mode waveform that has been extracted. If desired, a dispersion curve $f_m(t) = f_m(XS_g)$ can then be recovered from the single-mode waveform by estimating the local frequency as a function of time.

The remainder of this paper is organized as follows. In Section 2, we present a short derivation of the time-warping transform used in subsequent sections. In Section 3, the time-warping transform is applied to a synthetic seismogram. In Section 4, the time warping transform is applied to a measured seismogram. In Section 5, we summarize and discuss our results.

2 TIME-WARPING

In this section, we have two objectives: (1) present a self-contained explanation of the mathematics underlying time-warping and (2) apply these results to a particular environment, thereby defining the time-warping transform that is used in the two sections that follow. The warping transform used here is essentially the same transform that is described in Brown (2019), but all details are different because the environments are different.

The environment assumed here is a slightly modified no-ocean isotropic PREM (Preliminary Reference Earth Model) (Dziewonski & Anderson 1981). The starting point is PREM with Earth radius 6371 km but with the ocean replaced by upper crust with a maximum shear wave speed of 3.0 km s^{-1} at the surface. A Cartesian coordinate system is used so a preliminary step is application of the Earth flattening transformation of Biswas & Knopoff (1970) ignoring the correction to the horizontal component of the wavenumber k; neglect of that correction is valid in the limit of large ka where a is Earth radius, and is consistent with our extensive use of asymptotic arguments when defining and applying the time-warping transformation. Application of the Earth-flattening transform results in a depth-dependent profile $V(z)$ of horizontal shear wave speed. We assume here that $V(z)$ varies linearly between grid points in the PREM model. Additionally, after Earth-flattening, a small amount of smoothing of the $V(z)$ profile is applied to improve numerical stability. With these comments in mind, the assumed environmental model for time-warping should be thought as a slightly smoothed PREM-like model. A stronger additional approximation is discussed below. Consistent with our focus on Love waves we assume that the measured dynamical variable is the transverse (relative to a great circle path) component of lateral ground motion velocity $v(t; X)$, where X is epicentral distance.

As noted in Brown (2019) only three simple results are needed to derive the time-warping transformation. First, Love waves are, to a good approximation, slowly varying linear wave trains, so $v(t, \mathbf{x}) = \mathrm{Re}[a(t, \mathbf{x}) \exp(i\phi(t, \mathbf{x}))]$, where $a(t, \mathbf{x})$ is a slowly varying amplitude and $\phi(t, \mathbf{x})$ is a rapidly varying phase. The local wave frequency and wavenumber are then

$$\omega = \frac{\partial \phi}{\partial t} \tag{1}$$

and $\mathbf{k} = -\nabla\phi$. Secondly, in a stratified environment with horizontal shear wave velocity $V(z)$ increasing with depth, Love wave normal modes asymptotically satisfy the dispersion (quantization) condition

$$\omega\tau(p_m) = 2\pi(m + \gamma), \tag{2}$$

where $\tau(p_m)$ is the reduced traveltime, m is mode number and p_m is the horizontal phase slowness, which is constant for each (m, ω)-pair. For modes with turning depths far from the core–mantle boundary $\gamma = 1/4$ (see, e.g. Dahlen & Tromp 1998). The appendix describes a uniform asymptotic description of a Love wave modal expansion, including a derivation of eq. (2) that provides a means to generalize that result. The third required result is that, because wave energy travels at the group slowness, traveltimes satisfy

$$t = S_g(p_m)X, \tag{3}$$

where the independent variable X (with no argument) is epicentral distance. Eq. (3), with $S_g = \partial k_m/\partial\omega$ and $k_m = \omega p_m$, follows from a stationary phase evaluation of a Fourier integral representation of a fixed-m contribution to a seismogram, for example based on eq. (A9) after making use of the large argument asymptotic approximation to the Hankel function. Note that in the Appendix epicentral distance is denoted by r rather than X. We make use of an asymptotic approximation to evaluate S_g which is closely tied to eq. (2), $S_g(p_m) = T(p_m)/X(p_m)$, where $X(p_m) = -\mathrm{d}\tau/\mathrm{d}p_m$ is the horizontal single-cycle distance and $T(p_m) = \tau(p_m) + p_m X(p_m)$ is the corresponding traveltime. The independent variable X should not be confused with the dependent variable $X(p_m)$.

The time-warping transform follows from eqs (1) to (3). It is useful to define a second phase function φ by the relationship $\phi = 2\pi(m + \gamma)\varphi/\tau_{\mathrm{ref}}$ where τ_{ref} is an as yet unspecified constant with units of time. Note that ϕ, defined in eq. (1), is dimensionless, while φ has units time. It follows from eqs (1) and (2) and the definition of φ that

$$\omega = \frac{\partial\phi}{\partial t} = 2\pi\frac{m+\gamma}{\tau(p_m)} = 2\pi\frac{m+\gamma}{\tau_{ref}}\frac{\tau_{ref}}{\tau(p_m)} = 2\pi\frac{m+\gamma}{\tau_{ref}}\frac{\partial\varphi}{\partial t}.$$

It follows from the fourth equality in the equation above that $\partial\varphi/\partial t = \tau_{\mathrm{ref}}/\tau(p_m)$. Because (1) $t = S_g X$ and (2) $\partial/\partial t$ in the equations above is evaluated at fixed X, it follows that $\mathrm{d}\varphi/\mathrm{d}S_g = X\tau_{\mathrm{ref}}/\tau(p_m)$. $\tau(S_g)$ is defined parametrically, via $\tau(p)$ and $S_g(p)$. (The p_m are discrete values of the continuous variable p.) $\tau(p)$ is always single-valued but $p(S_g)$ need not be; if $p(S_g)$ is single-valued, then $\tau(S_g)$ is also single-valued. We assume that this condition is satisfied. Then we may integrate to give

$$\varphi(S_g) = X\tau_{\mathrm{ref}}\int_{S_o}^{S_g}\frac{\mathrm{d}S'}{\tau(S')}. \tag{4}$$

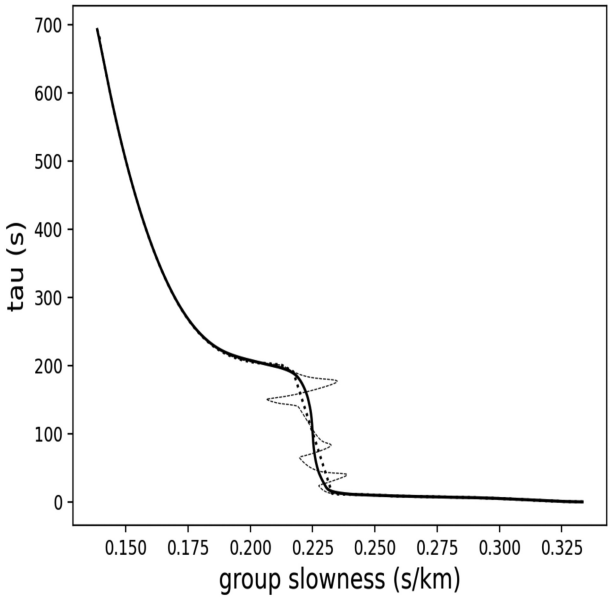

Figure 2. Reduced time τ versus group slowness S_g in the slightly smoothed no-ocean PREM model described in the text after application of the Earth-flattening transformation. The dashed curve corresponds to the unsmoothed $\tau(S_g)$ curve. The heavy solid and dotted curves correspond to two different *ad hoc* corrections to the unsmoothed $\tau(S_g)$ curve. The dotted curve is used only for a sensitivity test described in Section 3; all other time-warping-based processing results are based on the heavy solid curve.

S_o is a constant and $\varphi(S_o) = 0$; a good choice of S_o is the minimum value of S_g in the environment of interest. Eq. (4) defines $\varphi(S_g; X)$, but $t = S_g X$ so this equation defines $\varphi(t; X)$. Note that eq. (4) holds for all m and recall the relationship $\phi = 2\pi(m + \gamma)\varphi/\tau_{ref}$.

Suppose that, in a known environment at an experimentally relevant value of X, eq. (4) is evaluated so $\varphi(t)$ is known at that X. In addition, define the warped time t' by

$$t' = \varphi(t) \tag{5}$$

and assume that the seismogram at X is sampled uniformly in warped time t'. Then the corresponding warped radian frequencies are $\omega' = \partial\phi/\partial t' = (\partial/\partial t')((2\pi(m + \gamma)/\tau_{ref})t') = 2\pi(m + \gamma)/\tau_{ref}$. With this relationship in mind we choose $\tau_{ref} = 1$ s. Then warped frequency expressed in cycles per s is

$$f' = (m + \gamma)(1\,\text{Hz}). \tag{6}$$

If the measured seismogram consists of a superposition of contributions from many mode numbers m, the corresponding warped frequency spectrum will consist of many lines (whose widths are controlled by the length of the time-warped signal), consistent with the idealized behaviour shown in Fig. 1. The critical step in performing the time-warping transform is evaluation of the integral in eq. (4); to do so requires that $\tau(S_g)$ be single-valued.

Before completing our description of the warping transform we present numerical results for the assumed slightly smoothed no-ocean PREM model. τ versus S_g for that environmental model is shown in Fig. 2. The minimum value of S_g in Fig. 2 and elsewhere corresponds to the ray or mode whose turning depth grazes the core–mantle boundary. Because eq. (2) was derived assuming that modal turning depths are far from this interface, our numerical results are not valid for S_g values close to this minimum value. Fig. 2 was constructed by exploiting the parametric dependence, $\tau(p)$ and $S_g(p)$. Fig. 2 shows that $\tau(S_g)$ is not a single-valued function; in the approximate domain $0.215\,\text{s km}^{-1} < S_g < 0.235\,\text{s km}^{-1}$ there are two or more τ-values associated with each S_g. To evaluate the integral in eq. (4) and define the time-warping transform $\tau(S_g)$ must be single-valued. To correct the multivaluedness problem we have explored two options: (1) smooth $V(z)$; (2) apply a correction directly to $\tau(S_g)$. Our experience has shown option (2) is preferable and that the results of performing time-warping using such a localized correction are not sensitive to details of the correction that is applied. This statement is consistent with remarks made earlier about the relatively low sensitivity of the ideal shallow water waveguide time-warping transform to environmental mismatch. Unless otherwise noted, time warping results presented in this paper are computed with the correction shown in Fig. 2 with the solid curve. The corresponding *ad hoc* correction applied was $S_g(\tau) = a - b(\tau - \tau_0) - c(\tau - \tau_0)^3$ with $\tau_0 = 101.16$ s, $a = 0.225$ s km^{-1}, $b = 0.1592 \times 10^{-4}$ km^{-1}, $c = 0.8603 \times 10^{-8}$ s^{-2} km^{-1} for $12.57\text{ s} < \tau < 189.75$ s. It is important to appreciate that a price is paid for applying the correction to $\tau(S_g)$. We will return to this point below.

The left-hand panel of Fig. 3 shows φ versus S_g at $X = 8000$ km, computed by evaluating the integral in eq. (4). As noted above, converting $\varphi(S_g)$ to $\varphi(t)$ is a trivial stretching (relabeling of the S_g axis) because $t = S_g X$. The time-warping transform $t'(t)$, which is defined by setting $t' = \varphi(t)$, eq. (5), is illustrated graphically in the right panel of Fig. 3. Note that uniform sampling in t' involves non-uniform sampling in t, and vice versa. The warped-time sampling interval $\Delta t'$ is chosen so as to avoid aliasing in the warped-frequency f' domain. With the scaling that we have chosen ($\tau_{ref} = 1$ s) eq. (6) holds. We choose $\Delta t' = (2 \times 100\,\text{Hz})^{-1} = 0.005$ s corresponding to a Nyquist mode number of approximately 100. Because $t' = \varphi$ (eq. 5) and φ depends on epicentral distance X (eq. 4), our choice to use the same fixed value of $\Delta t'$ at all X dictates that the number of t' samples is proportional to X.

In addition to non-uniform sampling associated with the time-warping transform, an amplitude correction is applied whose purpose is to preserve the energy of the time-warped signal. Let $v(t)$ and $\bar{v}(t')$ denote the unwarped and warped signals, respectively, and let W and W^{-1} denote forward and inverse warping operators, respectively. Then $\bar{v}(t') = W[v(t)] = \sqrt{|dt/dt'|}v(t'(t))$ and $v(t) = W^{-1}[\bar{v}(t')] = \sqrt{|dt'/dt|}\bar{v}(t(t'))$.

The frequency spectrum of a time-warped seismogram consists of line-like features [recall eq. (6) and Fig. 1], each corresponding to a fixed mode number m. A bandpass filter can then be applied to isolate the contribution corresponding to a particular choice of m. Finally, applying the inverse warping transform, t' to t, yields the contribution to the original seismogram corresponding to that choice of m, that is a fixed mode number waveform.

3 APPLICATION TO SYNTHETIC SEISMOGRAMS

The synthetic seismograms used in this section were computed as a superposition of toroidal normal modes using the Mineos software package (Masters *et al.* 2011). The assumed environment was a no-ocean PREM, similar to the model described in the previous section but without the additional smoothing that is described in that section. Also, the *ad hoc* correction to $\tau(S_g)$ discussed in the previous section plays no role in the Mineos-based synthetics used here. In other words, the environment used to compute the Mineos-based synthetics is based on an earth model similar, but not identical, to the model used to define the time-warping transform. The synthetics used here are identical to the Love wave synthetics

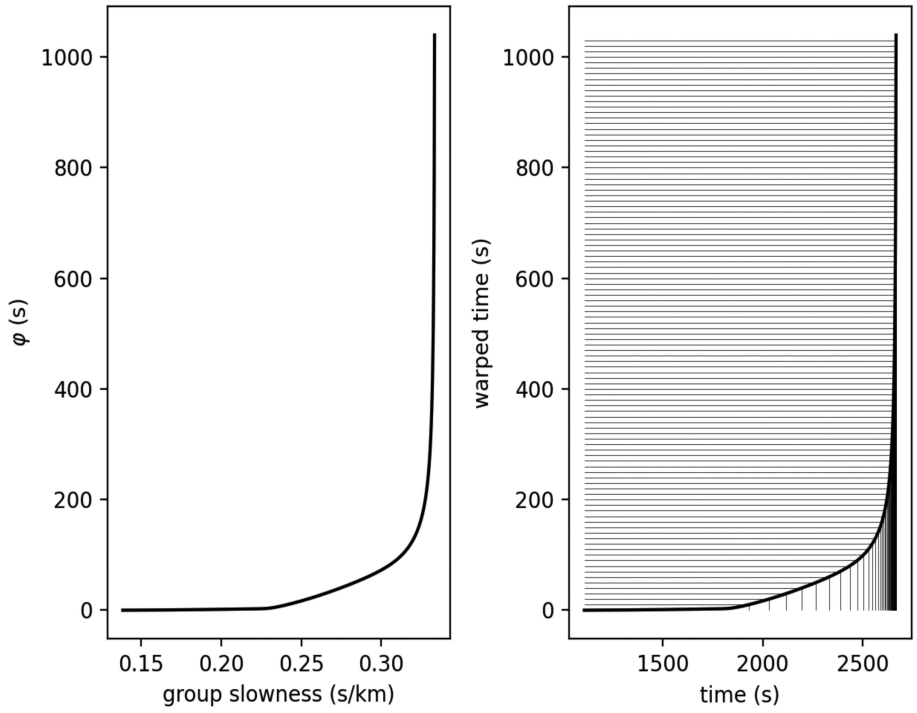

Figure 3. Left-hand panel: φ versus S_g at $X = 8000$ km, evaluated using eq. (4). Right-hand panel: graphical illustration of the time-warping transform $t'(t)$ at $X = 8000$ km.

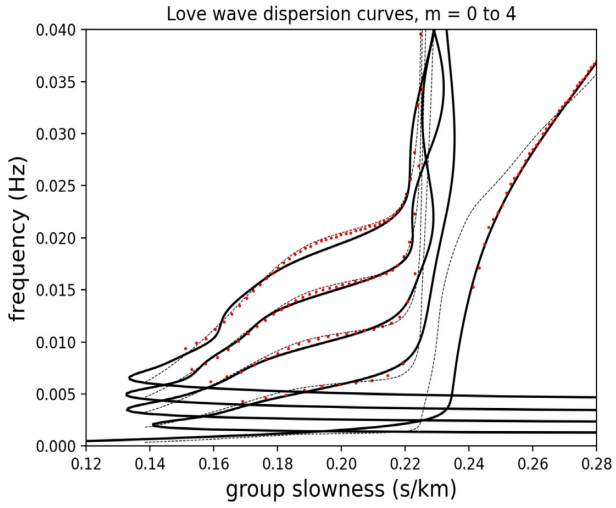

Figure 4. Heavy curves: exact dispersion curves for isotropic no-ocean PREM model computed using Mineos. Dashed curves: asymptotic dispersion curves based on an approximation to the no-ocean PREM model. The plotted red dots are time-warping-based estimates based on analysis of the synthetic seismogram at $X = 8000$ km shown in Fig. 5.

used in Matsuzawa & Yoshizawa (2019). These synthetics do not include any additive noise.

Fig. 4 shows two sets of dispersion curves. One set of curves is computed using Mineos using the assumed no-ocean isotropic PREM model. The other set of curves is computed using the approximate asymptotic results described in the previous section, making use of the modified $\tau(S_g)$ curve. [Given $\tau(S_g)$, dispersion curves are defined by eq. (2), with $\gamma = 1/4$.] The Mineos-based dispersion curves should be thought of as exact for the assumed PREM model and for the Mineos-based synthetics that we process in this section. The differences between the two sets of dispersion curves have simple explanations. The $m = 0$ curves at $S_g > 0.24$ s km^{-1} are sensitive to near surface structure; those curves are different due to the near-surface modification that we applied. The cause of the multivaluedness of the exact dispersion curves for $0.215\,\mathrm{s\,km^{-1}} < S_g < 0.235\,\mathrm{s\,km^{-1}}$ is the multivaluedness of $\tau(S_g)$ in that S_g domain (see Fig. 2); recall that we eliminated the multivalued structure to allow the time warping transform to be defined. (Without making the $\tau(S_g)$ modification shown in Fig. 2, the asymptotic dispersion curves closely match the exact dispersion curves in the corresponding S_g domain.) Finally, and most significantly, the asymptotic curves fail to reproduce the negative slope regions of the dispersion curves at very low f. The cause of this more serious shortcoming of the asymptotic results is that eq. (2) does not properly treat the core–mantle boundary, leading to errors for modes (at sufficiently low frequency and high mode numbers) with turning depths near this interface.

Some qualitative features of Fig. 4 are noteworthy. The limits on S_g in the asymptotic dispersion curves $[0.1385\,\mathrm{s\,km^{-1}}, 0.3333\,\mathrm{s\,km^{-1}}]$ impose limits on the time window within which Love wave energy is expected to arrive, $(0.1385\,\mathrm{s\,km^{-1}})(X) < t < (0.3333\,\mathrm{s\,km^{-1}})(X)$. This time window can be described as the Love wave time window. The fundamental mode ($m = 0$) dispersion curve is seen to extend over the entire S_g domain while all overtone energy corresponds approximately to $S_g < 0.235$ s km^{-1}. The $m = 0$ tail for $S_g > 0.235$ s km^{-1} looks rather insignificant in Fig. 4, but often most of the energy in measured seismograms is $m = 0$ energy. The significance of the temporal bounds on the overtone energy (assuming Fig. 4 is qualitatively correct) is that temporal bounds may be placed on seismograms to isolate overtone energy. Assuming the time-frequency structure shown in Fig. 4 (recall $t = S_g X$) is approximately correct, that structure can be exploited when processing seismograms by making use of a combination of bandpass filtering and time-gating. For

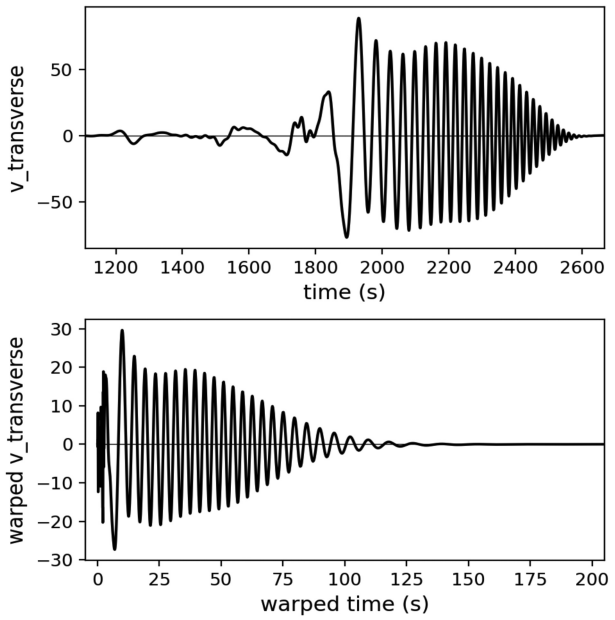

Figure 5. Upper panel: Synthetic seismogram for a no-ocean isotropic PREM model at $X = 8000$ km. Lower panel: corresponding time-warped synthetic seismogram. Only the early energetic portion of the time-warped seismogram is shown; at $X = 8000$ km warped time is defined for t' in excess of 1000 s as in Fig. 3.

example, because typically most of the overtone energy in seismograms is in the lowest overtones, much of the energy in the negative slope portion of the overtone dispersion curves that is not treated correctly in our asymptotic analysis can be removed by high-pass filtering seismograms, with a cut-off frequency of a few mHz. With these comments in mind we have imposed the following temporal bounds, with smooth tapers where appropriate, when processing both synthetic and measured seismograms: $(0.1385\,\mathrm{s\,km^{-1}})\,(X) < t < (0.3333\,\mathrm{s\,km^{-1}})\,(X)$ for the fundamental mode; $(0.1385\,\mathrm{s\,km^{-1}})\,(X) < t < (0.2400\,\mathrm{s\,km^{-1}})\,(X)$ for overtones. Also, we have high-pass filtered all seismograms with a cut-off frequency of 2.0 mHz. All filtering performed in this paper was done using the Python scipy.signal.sosfiltfilt function to eliminate spurious time-shifts.

The upper panel of Fig. 5 shows a synthetic seismogram at $X = 8000$ km for a source depth of 50 km in the Love wave time window, $(0.1385\ \mathrm{s\,km^{-1}})$ (8000 km) $< t <$ $(0.3333\ \mathrm{s\,km^{-1}})$ (8000 km). The lower panel shows the corresponding time-warped seismogram. The corresponding warped frequency power spectral density is shown in Fig. 6. According to eq. (6) with $\gamma = 1/4$ the warped frequency power spectral density should have peaks at $f' = (m + 1/4)$ (1 Hz). Indeed, spectral peaks are seen at these values of the warped frequency f' for m-values from 0 to 4. We shall focus our attention on those peaks. Other warped-frequency power spectral density peaks that are seen in Fig. 6 are discussed below. Before proceeding with the task isolating of energy corresponding to a fixed value of m we show results, similar to those in Fig. 5, but based on processing the same seismogram after time-windowing to isolate overtone energy.

Recall that Fig. 4 shows that overtone energy is expected to arrive at times less than approximately $(0.24\ \mathrm{s\,km^{-1}})\,(X)$. With that in mind, if our goal is to extract energy in one or more overtones, we may time-gate the original seismogram, excluding times greater than approximately $(0.24\ \mathrm{s\,km^{-1}})(X)$. Use of the time-gated time-series may be advantageous if the fundamental mode is so energetically

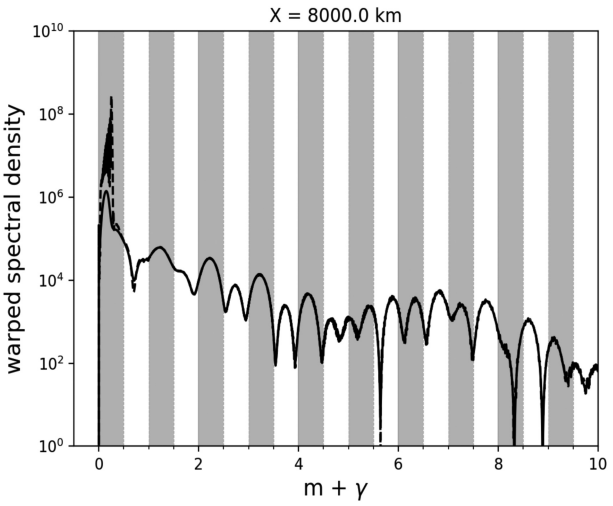

Figure 6. Power spectral density versus warped frequency, $f' = (m + \gamma)$ (1 Hz), corresponding to time-warped synthetic seismograms. Dashed curve: no taper applied to the seismogram prior to time-warping. Solid curve: taper applied to seismogram prior to time-warping. Shaded regions show the locations of expected spectral peaks for $\gamma = 1/4$.

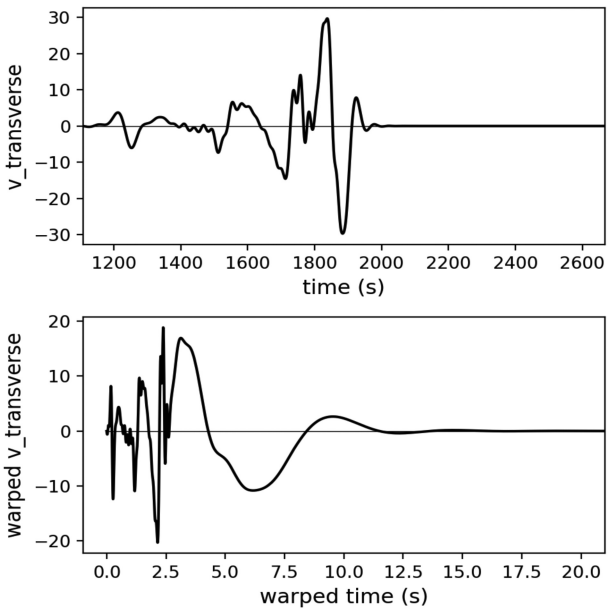

Figure 7. Same as Fig. 5 but computed using a time-windowed seismogram, as described in the text, to isolate contributions from overtones.

dominant that side lobes from the $m = 0$ peak in the warped frequency spectrum (shown in Fig. 6 and described later) interferes with, and possibly obscures, the overtone peaks. With this in mind, we have applied a taper to the seismogram and repeated the analysis shown in Fig. 5 using the tapered seismogram as a starting point. The applied taper, which effectively eliminates energy with $S_g > 0.24\ \mathrm{s\,km^{-1}}$, has temporal weighting $0.5\times[1 - \tanh((t - t_c)/t_w)]$ with $t_c = (0.235\ \mathrm{s\,km^{-1}})(\mathrm{X})$ and $t_w = (0.005\ \mathrm{s\,km^{-1}})\,(X)$. The tapered seismogram, before and after time-warping, is shown in Fig. 7. Fig. 6 shows warped spectral density corresponding to both untapered and tapered seismograms.

The warped frequency spectral density shown in Fig. 6 reveals several peaks at the expected locations, $f' = (m + 1/4)$ (1 Hz). The next processing steps are to select a value of m, bandpass filter

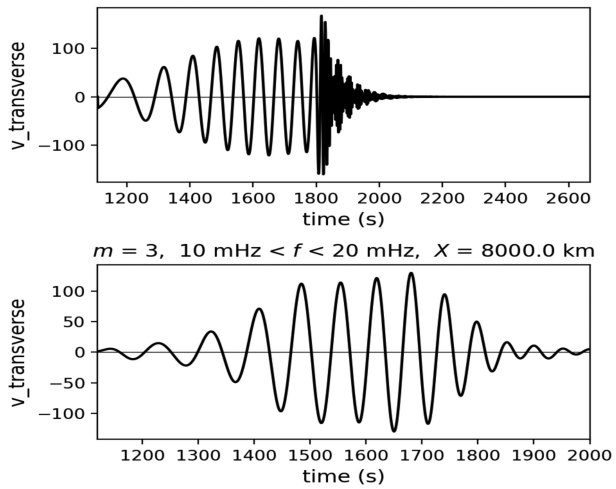

Figure 8. Upper panel: the time-warping-based estimate of the $m = 3$ waveform, $v_3(t; 8000\,\text{km})$, corresponding to the PREM model synthetic seismogram at $X = 8000$ km shown in the upper panel of Fig. 5. Lower panel: the same $m = 3$ waveform, $v_3(t; 8000\,\text{km})$ after bandpass filtering, $10\,\text{mHz} < f < 20\,\text{mHz}$.

the time-warped seismogram to extract the energy associated with that spectral peak, and perform an inverse time-warping transform to produce the relevant fixed-m waveform, $v_m(t; X)$. All bandpass filtering in the warped frequency domain performed in this paper uses cutoff frequencies of m +0.05 Hz and m +0.45 Hz; note that this band is centred at $(m + 1/4)$ (1 Hz).

$v_m(t; X)$ for $m = 3$, $X = 8000$ km is shown in the upper panel of Fig. 8. The analysis methods that we have applied do not properly treat the Airy phase at the leading edge of the waveform, so the early portion of the recovered waveform is not accurate. Also, recalling the comments made earlier about Fig. 2, we choose to focus on $t < 1760$ s. (1760 s = (0.22 s km^{-1})(8000 km) where 0.22 s km^{-1} is an approximate upper limit on S_g values that we expect to be negligibly affected by multivaluedness of $\tau(S_g)$.) Consistent with these restrictions, two related analysis methods can be applied. The simplest is to apply additional bandpass filtering of the $v_m(t; X)$ so as to strip out energy in those frequency bands that we don't have full confidence in. The choice of which frequency band to focus on for each m is based primarily on the dispersion curves shown in Fig. 4. An example of such a band-limited fixed-m waveform is shown in the lower panel of Fig. 8. Some energy is seen in that figure arriving later than the fuzzy upper bound of 1760 s that we have set, but most of that late arriving energy is due to diffractive smearing of energy in the 10–20 mHz passband.

A more complete set, corresponding to $m = 0$ through 4, of bandpassed $v_m(t; X)$ are shown in Fig. 9 together with Mineos-based synthetics of the same fixed-m waveforms. Agreement is seen to be good for all $m = 0$ through 4.

An alternative way to process time-warping-based estimates of $v_m(t; X)$ was alluded to earlier: construct dispersion curves by estimating the local frequency of the fixed-m broad-band waveform from the times between zero-crossings. For this purpose it is useful to make use of both the waveform and its Hilbert transform. This is a form of FTAN analysis mentioned earlier. The result of performing this analysis for $m = 0$, 1, 2, 3, 4 is shown by the points plotted in Fig. 4. For $m = 0$ all estimates correspond to S_g-values greater than approximately 0.235 s km^{-1}; agreement with Mineos-based dispersion curves for the isotropic PREM model is seen to be good. (Note that the data-based point estimates of $f(S_g)$ cluster

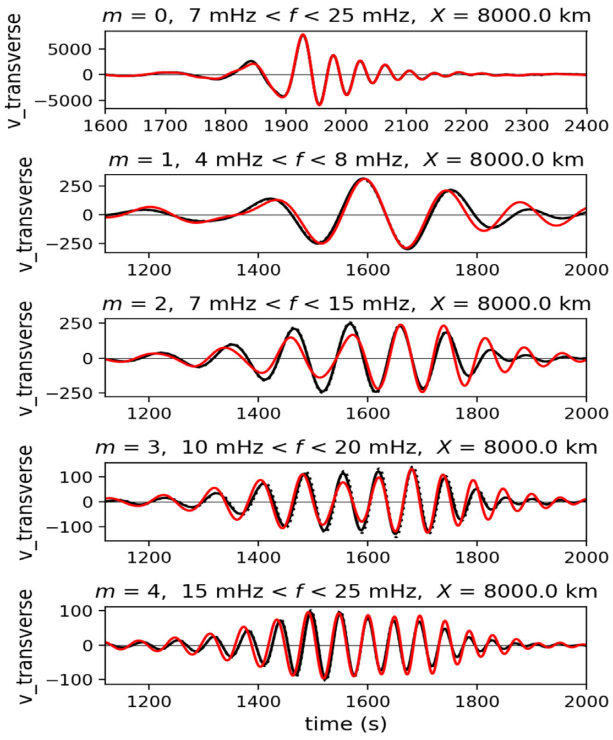

Figure 9. The solid black curve in each panel shows a band-limited fixed-m waveform $v_m(t; 8000\,\text{km})$ extracted from the seismogram shown in the upper panel of Fig. 5 using time-warping. The solid black $m = 3$ waveform is identical to that shown in the lower panel of Fig. 8. The dotted black curves show similar waveforms based on processing the same seismogram after adding noise as described in the text. The red curves are Mineos-based synthetics corresponding to the same band-limited fixed-m waveforms. In each panel the vertical scale for the solid black curve and the dotted black curve is identical; the vertical scale for each red curves is chosen so that peak amplitudes for red and black solid curves are the same.

around the correct dispersion curve for the underlying PREM model and not the slightly different dispersion curve corresponding to the model that was used to define the time-warping transform.) For $m = 1$, 2, 3, 4 all f-estimates for S_g-values less than approximately 0.22 s km^{-1} are seen to be in fairly good agreement with PREM-based values. Estimates of $f(S_g)$ in the region where theoretical curves are not single-valued are not in agreement with theoretical curves, however. This behavior is expected because to derive the time-warping transform it was assumed that eq. (2) with constant γ is valid and that $\tau(S_g)$ is single-valued. With these assumptions dispersion curves $f(t)$ [or $f(S_g)$] must also be single-valued. This follows from the observation that single-valuedness of $f(S_g)$ requires that $\mathrm{d}S_g/\mathrm{d}f$ is everywhere non-zero and

$$\frac{\mathrm{d}S_g}{\mathrm{d}f} = \frac{\mathrm{d}S_g}{\mathrm{d}\tau}\frac{\mathrm{d}\tau}{\mathrm{d}f} = -\frac{\mathrm{d}S_g}{\mathrm{d}\tau}\frac{m+\gamma}{f^2}. \tag{7}$$

The second equality follows from eq. (2) with m fixed and constant γ. Thus, with the assumptions that we have made, zeros of $\mathrm{d}S_g/\mathrm{d}\tau$ coincide with zeros of $\mathrm{d}S_g/\mathrm{d}f$, so single-valuedness of $\tau(S_g)$ implies single-valuedness of $f(S_g)$ for all m. As a consequence of this limitation, for the PREM-based synthetics analysed here we don't have confidence in dispersion curve estimates in the approximate range $0.215\,\text{s km}^{-1} < S_g < 0.235\,\text{s km}^{-1}$. The beating behavior seen in the $m = 3$ waveform shown in the upper panel of Fig. 8 at times greater than approximately 1800 s is a manifestation of our time warping operator failing for this band of S_g-values.

For the same event, with a source depth of 50 km, we have processed seismograms at epicentral distances X of 6000 and 10 000 km. Results are essentially identical to those described above for $X = 8000$ km. A small difference in results at the three values of X is that the length of the warped-time time-series is proportional to X. As a result, warped frequency spectral resolution, for example in Fig. 6, improves with increasing X.

At all three values of X results for a (synthetic) event at a depth of 200 km led to results that are clearly inferior to results at the same X corresponding to a source depth of 50 km. This suggests that a shallow source is advantageous for Love wave time-warping. This issue will be discussed below.

To investigate sensitivity to noise we have added Gaussian white noise to the synthetic seismogram shown in the upper panel of Fig. 5 and repeated the time-warping-based processing. Fixed-m waveforms corresponding to a temporally integrated SNR of 20 dB are shown in Fig. 9. Results are nearly identical to the no-noise fixed-m waveforms, suggesting robustness to moderate additive noise. Note that, because seismogram energy is mostly in the $m = 0$ mode and the 20 dB measure of SNR is based on time-integrated measures of signal and noise levels, the effective SNR is greater than 20 dB for $m = 0$ and less than 20 dB for $m \geq 1$.

We have noted that the warped-frequency spectral density shown in Fig. 6 is expected to have narrow peaks (widths are approximately equal to the reciprocal of the length of the energetic portion of the warped time-series) at warped frequencies equal to $(m + 1/4)$ (1 Hz). Those peaks are indeed seen in Fig. 6 for $m = 0$, 1, 2, 3, 4 and possibly slightly higher m-values. But Fig. 6 also shows peaks at other frequencies. Those spurious peaks are not consistent with eq. (2) with $\gamma = 1/4$, the result derived in the Appendix. The cause of the spurious peaks and the fact that the $m + 1/4$ peak pattern is clear only for small m is likely tied to the incorrect treatment in the Appendix of the boundary condition at the core–mantle boundary. eq. (2) with $\gamma = 1/4$ does not hold at very low frequencies and/or high mode numbers, that is for modes with turning depths at or near the core–mantle boundary. For high-angle modes that reflect off the core–mantle boundary eq. (2) holds with $\gamma = 0$; see table 12.1 in Dahlen & Tromp (1998). Replacement of $\gamma = 1/4$ by $\gamma = 0$ does not account for the spurious peaks in Fig. 6. It may be possible to explain those peaks as transitional between non-reflecting and reflecting modes, as outlined in the Appendix, but for those transitional modes the dispersion relation will be considerably more complicated than eq. (2) with a constant value of γ.

4 APPLICATION TO MEASURED SEISMOGRAMS

In this section, we present time-warping results for a seismogram corresponding to the 2019 M_w 7.1 Ridgecrest earthquake in California (http://ds.iris.edu/ds/nodes/dmc/tools/event/11058875). The seismogram analysed here was based on measurements made at the PM.ROSA seismic station on São Jorge Island in the Azores, downloaded from the Incorporated Research Institutions for Seismology (IRIS). The epicentral distance is $X = 7573.53$ km. The time-warping transform used here is the transform described in Section 2 based on the isotropic PREM model described in that section. Consistent with our use of this model to define the time-warping transform, we assume that the dispersion characteristics of the measured seismogram and the qualitative features of the underlying earth model are as described above.

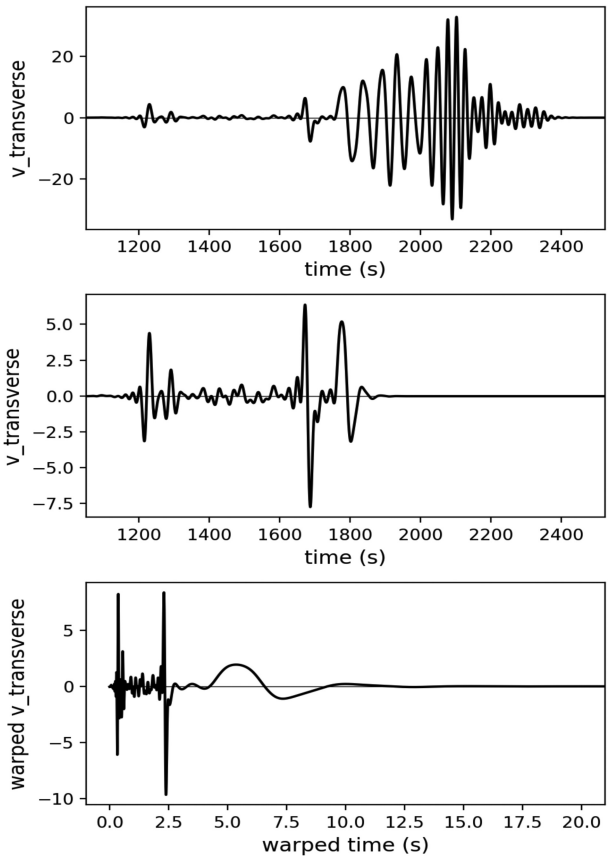

Figure 10. Upper panel: ridgecrest event seismogram (transverse horizontal velocity) in the Love wave time window at the PM.ROSA station; $X = 7573.53$ km. Middle panel: same seismogram after applying a taper to isolate overtone contributions. Lower panel: time-warped seismogram corresponding to the unwarped seismogram shown in the middle panel. Only the early energetic portion of the time-warped seismogram is shown; at $X = 7573.53$ km warped time is defined for t' as large as approximately 1000 s as in Fig. 3.

The upper panel of Fig. 10 shows the PM.ROSA record of transverse horizontal ground velocity in the Love wave time window for the Ridgecrest event. The corresponding tapered seismogram that isolates Love wave overtone contributions is shown in the middle panel. The same X-dependent taper that was applied to the synthetic seismogram in the previous section was used here. The time-warped seismogram corresponding to the tapered seismogram is shown in the lower panel. As was the case in Figs 5 and 7, only the early energetic portion of the time-warped seismogram is shown in Fig. 10.

Fig. 11 shows warped frequency spectral density corresponding to time-warped seismograms, both without and with tapering applied prior to time-warping. As was the case for the synthetic seismogram analysed in the previous section (recall Fig. 6), in Fig. 11 the taper is seen to remove most of the fundamental mode energy while leaving unchanged the overtone energy. This similarity between Figs 6 and 11 gives us confidence that the dispersion characteristics of the synthetic and measured seismograms are qualitatively similar.

Fig. 11 shows that the warped spectral density has peaks at the expected locations, where $f' = (m + 1/4)(1\,\text{Hz})$ for $m = 0$, 1, 2, 3, 4; additional spectral peaks are discussed below. As in the previous section, the next steps to isolate the corresponding fixed-m waveform, $v_m(t; X)$, are to choose a value of m, apply a narrow bandpass filter to the time-warped seismogram to isolate the energy

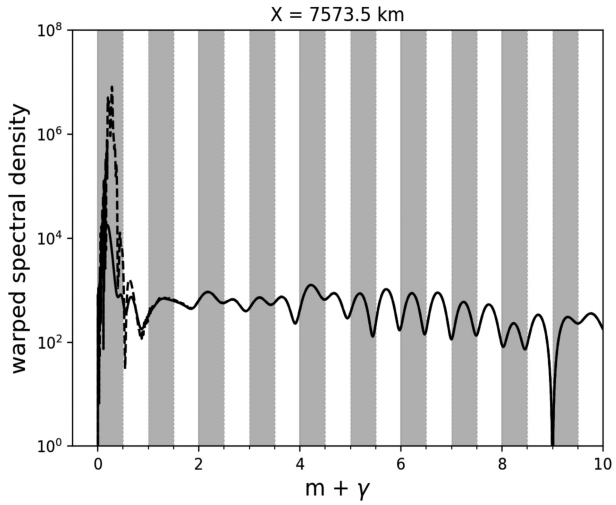

Figure 11. Power spectral density versus warped frequency, $f' = (m + \gamma)$ (1 Hz), corresponding to time-warped seismograms. Dashed curve: no taper applied to the seismogram prior to time-warping. Solid curve: taper applied to seismogram prior to time-warping. Shaded regions show the locations of expected spectral peaks for $\gamma = 1/4$.

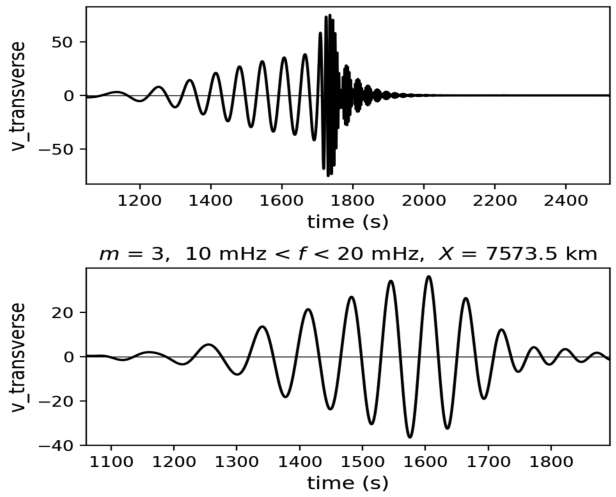

Figure 12. Upper panel: the $m = 3$ waveform, $v_3(t; 7573.53\,\text{km})$, corresponding to the seismogram at $X = 7573.53$ km shown in the middle panel of Fig. 10. Lower panel: the same $m = 3$ waveform, $v_3(t; 7573.53\,\text{km})$ after bandpass filtering, $10\,\text{mHz} < f < 20\,\text{mHz}$.

at that value of m, and then apply an inverse warping transform, t' to t. Note that to construct the $m = 0$ waveform $v_0(t; X)$ the entire seismogram (without taper applied) is used prior to time-warping. An example of $v_m(t; X)$ corresponding to $m = 3$, is shown in the upper panel of Fig. 12. The lower panel of the same figure shows a band-limited version of $v_3(t; X)$. As was the case when discussing Fig. 8, the reason for applying the final bandpass filter is to focus on the energy in which we have the greatest confidence.

Bandpassed $v_m(t; X)$, estimated using time-warping, for $m = 0$ through 4 are shown in Fig. 13. Unlike Fig. 9, fixed-m band-limited synthetics are not shown in this figure. The reason is that, unlike Fig. 9, the underlying earth model is not known. The qualitative similarity between Figs 9 and 13 suggest, however, that the time-warping-based estimates of $v_m(t; X)$ shown in Fig. 13 are correct and that the underlying earth model does not deviate significantly from PREM. One could use differences between the $v_m(t; X)$ shown

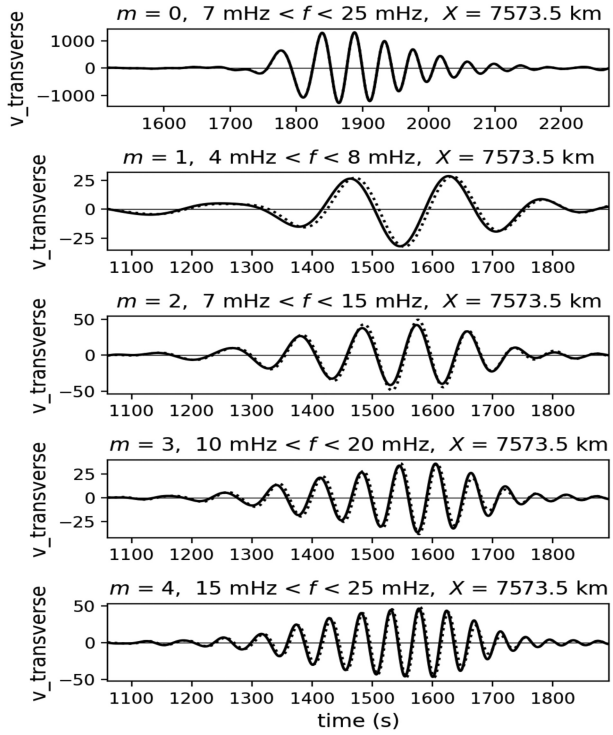

Figure 13. Band-limited fixed-m waveforms $v_m(t; 7573.5\,\text{km})$ extracted from the seismogram shown in Fig. 10 using time-warping. Solid and dotted curves correspond to warping transforms based on the solid and dotted curves, respectively, shown in Fig. 2. The $m = 3$ solid curve is identical to that shown in the lower panel of Fig. 12.

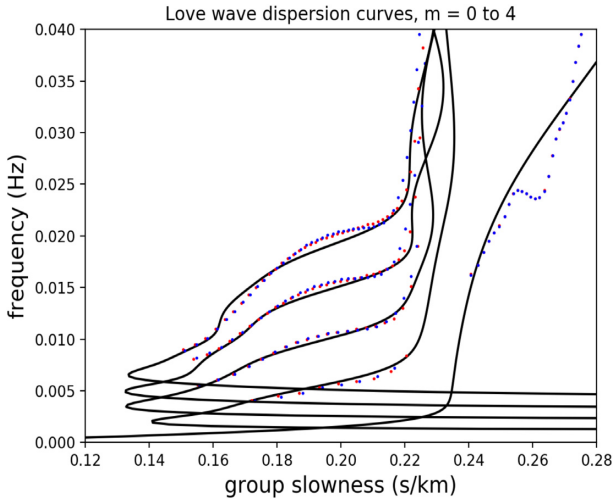

Figure 14. Heavy curves: exact dispersion curves for isotropic no-ocean PREM model computed using Mineos. The same curves are shown in Fig. 4. The plotted dots, both red and blue, are based on time-warping analysis of the seismogram at $X = 7573.53$ km shown in Fig. 9. Red and blue dots correspond to warping transforms based on the solid and dotted, respectively, $\tau(S_g)$ curves shown in Fig. 2.

in Fig. 13 and PREM-based synthetics as the basis for an inversion algorithm.

As was done in the previous section, points on dispersion curves can be estimated from the times between successive zero-crossings of the fixed-m waveforms $v_m(t; X)$ and their Hilbert transforms. Fig. 14 shows those measurement-based points together with theo-

retical (as computed by Mineos) dispersion curves for the isotropic PREM model. The theoretical dispersion curves shown in Fig. 14 are identical to those shown in Fig. 4. The approximate agreement between PREM-based theoretical dispersion curves and the seismogram-based estimates of points on those curves is indicative that (1) the underlying earth model does not differ significantly from the assumed PREM model and (2) the time-warping processing is performing as it is intended to.

The cause of the beats in the high frequency tail of the waveform shown in the upper panel of Fig. 12 is that the local frequency $f_3(t)$, estimated as just described, does not increase monotonically for t greater than about 0.225 s km^{-1} X. The same behavior is observed in the $m = 1$, 2 and 4 waveforms. As was the case in our analysis of PREM-based synthetics in the previous section, we interpret this behaviour as an indication that, within a narrow band of S_g-values near 0.225 s km^{-1}, the underlying earth model violates the assumed condition that $\tau(S_g)$ is single-valued. For that reason we do not have confidence in time-warping-based estimates of $f(S_g)$ for S_g-values near 0.225 s km^{-1}.

It is natural to ask how sensitive time-warping-based estimates of fixed-m waveforms and dispersion curves are to the choice of the reference model used to define the warping transform. This was not done in the previous section where the focus was on comparing time-warping-based estimates of fixed-m waveforms to synthetics. Of particular interest in regard to sensitivity to the reference model is the somewhat arbitrary manner that $\tau(S_g)$ (recall Fig. 2) was modified to be single-valued. To investigate this issue a different modified model was used to define the warping transform and all processing steps were repeated. The modified model, which is shown in Fig. 2, used a linear correction, $S_g(\tau) = a - b(\tau - \tau_0)$ with $\tau_0 =$ 101.79 s, $a = 0.225$ s km^{-1}, $b = 0.8754 \times 10^{-4}$ km^{-1} for 12.57 s $< \tau <$ 191.01 s. Also, the additional smoothing that was used in the reference model described earlier was not applied in the modified model. Fixed-m waveforms and dispersion curves constructed using the modified reference model are shown in Figs 13 and 14, respectively. Results are seen to be nearly identical to results based on the previously described reference model. We emphasize that neither choice of $\tau(S_g)$ overcomes the requirement that $\tau(S_g)$ be everywhere single-valued, and for both choices we do not have confidence in results corresponding to S_g values in the approximate range 0.215 s km^{-1} $< S_g <$ 0.235 s km^{-1}. It is nevertheless reassuring that extracted waveforms and dispersion curves do not exhibit strong sensitivity to the assumed reference model.

The test just described does not focus on sensitivity to the near-surface structure in the reference model used to define the warping transform. The fundamental mode is most sensitive to this structure as evidenced by Fig. 4, where it is seen that asymptotic dispersion curves (based on a smoothed near-surface structure) differ appreciably from exact dispersion curves only for $m = 0$. But Fig. 4 suggests that use of a smoothed near-surface structure to define the warping transform does not result in a biased $m = 0$ dispersion curve estimate. When analysing the Ridgecrest earthquake we don't know the correct dispersion curves or the correct near-surface structure, but the following argument strongly suggests that the time-warping-based estimates of points on the $m = 0$ dispersion curve shown in Fig. 14 are not subject to a bias associated with a poor choice of the reference model. Because all energy with $S_g >$ 0.24 s km^{-1} is expected to be $m = 0$ energy we can estimate the $m = 0$ dispersion curve independent of time-warping by applying our version of FTAN analysis after time-windowing the measured seismogram. Results (not shown) are nearly identical to the time-warping-based estimates shown in Fig. 14. These arguments suggest that an approximate near-surface reference model such as the one used here should work well in teleseismic applications. A reference model with more accurate crustal and Moho structure may be needed for regional studies.

In principle, an ocean layer can be handled by applying the traction-free boundary condition at the seafloor. There may, however, be associated practical challenges that we have not considered here. These include: (1) proper treatment of a soft sediment layer; (2) observational challenges associated with noisy horizontal motion components measured on broadband ocean-bottom seismometers and (3) possible enhancement (relative to continental structure) of the SH low-velocity structure in the asthenosphere under the oceanic lithosphere. The latter issue is tied to the condition that $\tau(S_g)$ must be single valued to define the time-warping transform.

Fig. 11 reveals peaks both at expected locations, $f' = (m + 1/4)$ (1 Hz) for integer m, and at unexpected locations. The $m + 1/4$ peaks for $m = 2$ and 3 are not a strong as those seen in Fig. 6 (for the synthetic), but there are resolved peaks at the locations predicted by theory. Both figures show a hint that the $m + 1/4$ pattern of peaks extends to $m = 5$ and larger. Also, in both figures there are peaks at f' values that differ from the predicted peak locations, $f' = (m + 1/4)$ (1 Hz). The origin of those peaks is not clear. Figs 6 and 11 have both (1) many features that are consistent with the simple theoretical arguments we have given and (2) some unexplained features.

We have performed a time-warping analysis of the same event using seismograms measured at other locations. Results are consistent with but inferior to (e.g. fewer resolved peaks in warped-frequency spectral density plots at expected locations) results reported here. This behavior may be due to local structure near the measurement locations.

We have also performed a time-warping analysis of seismograms at several locations corresponding to the 2021 M_w 7.1 Honshu event (http://ds.iris.edu/ds/nodes/dmc/tools/event/11377253). Results were much less favorable than those corresponding to the Ridgecrest event. The Ridgecrest event was unusually shallow, with depth estimates ranging from 4 to 9 km (Lin 2020; Lomax 2020; Wang *et al.* 2020), while the Honshu event was a deep subduction zone event, at a depth of about 50 km (IRIS location). As was the case with the our analysis of synthetics, the source depth—and perhaps, more generally, source dynamics—seems to be an important factor that controls whether time-warping will work well or not.

5 DISCUSSION

We have shown that fixed-m Love wave waveforms and corresponding dispersion curves can be recovered from a seismogram measured at an isolated location using time-warping techniques. This statement is based on several observations. First, the warped frequency spectral density shown in Figs 6 and 11 reveals peaks at those locations predicted by theory, $f' = (m + 1/4)$ (1 Hz) for $m = 0$ through 4. Secondly, the recovered dispersion curves shown in Figs 4 and 14 are in agreement with PREM dispersion curves excluding the S_g band where we have argued that time-warping is expected to fail. And third, the agreement shown in Fig. 9 between fixed-m waveforms extracted using time-warping and Mineos-based fixed-m synthetics is good. While we have no proof that the corresponding measurement-based fixed-m waveforms shown in Fig. 13 are correct, all indications are that these waveforms can be trusted and used as the basis for an inversion algorithm. Not surprisingly, time-warping as implemented here also has some shortcomings, some of which will now be discussed. It is important to keep in mind that

the problem of extracting fixed-m waveforms from a seismogram measured at an isolated station is extremely challenging. Overall, our assessment of time-warping as implemented here is that it is an imperfect tool, but a useful tool.

Time-warping as implemented here is subject to a set of modest geometric constraints. Like many other widely used seismic methods we have assumed a 1-D earth model which precludes treatment of lateral structure and deviations from propagation along great circle paths. This assumption is somewhat restrictive, but remains a good approximation in many applications. Also, to use the methods described here it is advantageous to choose time windows that isolate Love wave energy. This places restrictions on epicentral distance.

The results that we have described suggest that a shallow source is advantageous for Love wave time-warping. A plausible explanation for this is that in the frequency band that we have focused on, roughly 5–25 mHz, toroidal Earth modes for mode numbers less than approximately 5 have no nodes at depths shallower than about 50 km. Thus, those mode numbers are expected to be excited across the entire 5–25 mHz frequency band provided the source depth does not exceed approximately 50 km. In contrast, a deeper source will lie near the first node for some mode numbers at some frequencies, leading to poor, or at least non-uniform in frequency, excitation of energy with those mode numbers. This argument is expected to apply robustly in the sense of being independent of details of source dynamics because, independent of those details, the same modal depth structure weighting applies.

In underwater acoustic applications of time-warping (Bonnel *et al.* 2020) argue that deconvolution—correcting for a non-impulsive source function—is a useful pre-processing step, for instance when the acoustic source is an underwater explosion with a known time history including bubble pulse oscillations. The same pre-processing could be applied to seismic data. We have chosen not to pursue that issue here because of concerns relating to uncertainty of the seismic source time history.

The time-warping results that we have presented are based on eq. (2) and some of the shortcomings that we have mentioned are tied to shortcomings of that equation. The principle weakness of eq. (2), which is derived in the Appendix, is the lower boundary condition (at $z \rightarrow -\infty$) that was assumed. Use of this approximate boundary condition precludes proper treatment of the core–mantle boundary and, in particular, energy reflecting from this boundary back into the mantle. As outlined in the Appendix, a more accurate dispersion relationship could be derived without too much difficulty. The improved dispersion relation would, however, likely not lead to a warping transform that could be implemented as described here. This topic is may be worth pursuing, even if it doesn't result in an improved time-warping transform, because this exercise could explain the origin of the warped frequency spectral peaks that we have observed at locations other than $f' = (m + 1/4)$ (1 Hz). Using the time-warping transform that we have described and implemented, we have shown that it is possible to avoid shortcomings of eq. (2) by focusing on m-dependent frequency bands within which eq. (2) is a good approximation. It should be understood, however, that our use of a time-warping transform based on eq. (2) as a mantle imaging tool leads to a blind spot near the core–mantle boundary.

Another shortcoming of the time-warping transform that we have described is the restriction that $\tau(S_g)$ be single-valued. As we have seen, that condition is violated in the assumed isotropic PREM model. We satisfied the condition by making an *ad hoc* correction that forced $\tau(S_g)$ to be single-valued. The *ad hoc* correction allows a time-warping transform to be defined but does not eliminate all potential problems; if the single-valuedness condition is violated in the environment in which measurements are made (which of course may be different from the isotropic PREM model), time-warping-based processing should be expected to produce spurious results for S_g values within the domain in that environment over which $\tau(S_g)$ is not single-valued. Our synthetic seismogram numerical results strongly suggest that, while errors are present, those errors are isolated within the band of S_g-values over which $\tau(S_g)$ is not single-valued. Similar results were observed in our analysis of measured seismograms, suggesting that the corresponding mantle structure is associated with a multivalued $\tau(S_g)$ structure similar to that in the isotropic PREM model. The associated physical domain is the mantle transition zone. As was the case when dealing with shortcomings of eq. (2), errors can be eliminated by applying bandpass filters that eliminate waveform energy that we don't have full confidence in. In this case, the price paid is that we have limited ability to image details of the mantle transition zone. As a practical matter, this is a more significant shortcoming than limited ability to image structure near the core–mantle boundary.

We have made no attempt here to account for attenuation-induced dispersion (Kanamori 1977). We do not expect this to be a significant factor limiting the validity of our time-warping results, but the issue is worthy of further investigation. These effects are accounted for in the Mineos-based dispersion curves shown in Figs 4 and 14. We have attributed some of the differences between our dispersion curves and those predicted by Mineos to smoothing of our PREM-like model and our use of asymptotic theory, but attenuation-induced dispersion could also be a contributing factor.

To put the present study in a broader context, it is important to mention alternative methods that have proven to be useful to extract fixed-m (including overtone) waveforms for Love waves. Array processing methods (see Matsuzawa & Yoshizawa 2019,and references therein) offer an attractive alternative to achieve the same goal, but those methods can be used only when a fairly dense array of receiving stations is present. An alternative approach is to make use of waveform fitting and stripping methods (van Heijst & Woodhouse 1997; Yoshizawa & Kennett 2002; Beucler *et al.* 2003; Visser *et al.* 2007; Yoshizawa & Ekström 2010). Those methods do not require an array of receiving stations and avoid some of the restrictions associated with time-warping that we have described, but they have the disadvantage that the source function must be known to compute accurate synthetics, which is critical to the fitting and stripping algorithm. Thus, in spite of some shortcomings of time-warping as described here, this method offers a viable alternative to other available methods to isolate fixed-m Love wave waveforms.

ACKNOWLEDGMENTS

The work of MGB was supported by the US Office of Naval Research, grant N00014-21-1-2511.

DATA AVAILABILITY

Seismic data were downloaded through the IRIS Wilber 3 system (https://ds.iris.edu/wilber3/) for the seismic network PM (Instituto Portugues Do Mar E Da Atmosfera 2006).

REFERENCES

Ahluwalia, D.S. & Keller, J.B., 1977. Exact and asymptotic representations of the sound field in a stratified ocean, in *Wave Propagation and Underwater Acoustics, Lecture Notes in Physics,* Vol. **70,** pp. 14–85, eds Keller, J.B. & Papadakis, J.S., Springer.

Baraniuk, R.G. & Jones, D.L., 1995. Unitary equivalence: a new twist on signal processing, *IEEE Trans. Signal Process.,* **43,** 2269–2282.

Beucler, É., Stutzmann, É. & Montagner, J.-P., 2003. Surface wave higher-mode phase velocity measurements using a roller-coaster-type algorithm, *Geophys. J. Int.,* **155,** 289–307.

Biswas, N. & Knopoff, L., 1970. Exact Earth-flattening calculation for Love waves, *Bull. seism. Soc. Am.,* **60,** 1123–1137.

Bonnel, J. & Chapman, N.R., 2011. Geoacoustic inversion in a dispersive waveguide using warping operators, *J. acoust. Soc. Am.,* **130,** EL101–EL107.

Bonnel, J., Nicolas, B., Mars, J.I. & Walker, S.C., 2010. Estimation of modal group velocities with a single receiver for geoacoustic inversion in shallow water, *J. acoust. Soc. Am.,* **128,** 719–727.

Bonnel, J., Gervaise, C., Roux, P., Nicolas, B. & Mars, J., 2011. Modal depth function estimation using time-frequency analysis, *J. acoust. Soc. Am.,* **130,** 61–71.

Bonnel, J., Dosso, S.E. & Chapman, N.R., 2013. Bayesian geoacoustic inversion of single hydrophone light bulb data using warping dispersion analysis, *J. acoust. Soc. Am.,* **134,** 120–130.

Bonnel, J., Thode, A., Wright, D. & Chapman, N.R., 2020. Non-linear time-warping made simple: a step-by-step tutorial on underwater acoustic modal separation with a single hydrophone, *J. acoust. Soc. Am.,* **147,** 1897–1926.

Brown, M.G., 2019. Time-warping in underwater acoustic waveguides, *J. acoust. Soc. Am,* **147,** 898–910.

Brown, M.G., Godin, O.A., Zang, X., Ball, J.S., Zabotin, N.A., Zabotina, L.Y. & Williams, N.J., 2016. Ocean acoustic remote sensing: results from the Florida Straits, *Geophys. J. Int.,* **206,** 574–589.

Dahlen, F.A. & Tromp, J., 1998. *Theoretical Global Seismology,* pp. 1025, Princeton Univ. Press.

Duan, R., Chapman, N.R., Yang, Y. & Ma, Y., 2016. Sequential inversion of modal data for sound attenuation in sediment at the New Jersey Shelf, *J. acoust. Soc. Am.,* **139,** 70–84.

Dziewonski, A.H. & Anderson, D.L., 1981. Preliminary reference Earth model, *Phys. Earth planet. Inter.,* **25,** 297–356.

Dziewonski, A.M. & Hales, A.L., 1972. Numerical analysis of dispersed seismic waves, in *Methods in Computational Physics,* Vol. **11,** pp. 39–85, ed. Bolt, B., Academic Press.

Ekström, G., Tromp, J. & Larson, E.W.F., 1995. Measurements and global models of surface wave propagation, *J. geophys. Res.,* **102,** 8137–8157.

Forsyth, D.W. & Li, A., 2005. Array analysis of two-dimensional variations in surface wave phase velocity and azimuthal anisotropy in the presence of multipathing interference, in *Seismic Earth: Array Analysis of Broadband Seismograms, Geophysical Monograph,* Vol. **157,** pp. 81–97, Am. Geophys. Un.

Foster, A., Ekström, G. & Nettles, M., 2014a. Surface wave phase velocities of the Western United States from a two-station method, *Geophys. J. Int.,* **196,** 1189–1206.

Foster, A., Nettles, M. & Ekström, G., 2014b. Overtone interference in array-based Love wave phase measurements, *Bull. seism. Soc. Am.,* **104,** 2266–2277.

Godin, O.A., Katsnelson, B.G. & Tan, T.W., 2019. Normal mode dispersion and time-warping in the coastal ocean, *J. acoust. Soc. Am.,* **146,** EL205–EL211.

Hamada, K. & Yoshizawa, K., 2015. Interstation phase speed and amplitude measurements of surface waves with nonlinear waveform fitting: application to USAaray, *Geophys. J. Int.,* **203,** 1463–1482.

Instituto Português do Mar e da Atmosfera, I.P.. 2006. *Portuguese National Seismic Network* [Data set]. International Federation of Digital Seismograph Networks. https://doi.org/10.7914/SN/PM.

Kanamori, H., 1977. Importance of physical dispersion in surface wave and free oscillation problems: review, *Rev. Geophys. Space Phys.,* **15**(1), 105–112.

Le Touzé, G., Nicolas, B., Mars, J. & Lacoume, J., 2009. Matched representations and filters for guided waves, *IEEE Trans. Signal Process.,* **57,** 1783–1795.

Levshin, A.L., Pisarenko, V.F. & Pogrebinsky, G.A., 1972. On a frequency-time analysis of oscillations, *Ann. Geophys.,* **28,** 211–218.

Lin, F.C. & Ritzwoller, M.H., 2011. Helmholtz surface wave tomography for isotropic and azimuthally anisotropic structure, *Geophys. J. Int.,* **186,** 1104–1120.

Lin, F.C., Ritzwoller, M.H. & Sneider, R., 2009. Eikonal tomography: surface wave tomography by phase front tracking across a regional broadband seismic array, *Geophys. J. Int.,* **177,** 1091–1110.

Lin, G., 2020. Waveform cross-correlation relocation and focal mechanisms for the 2019 Ridgecrest earthquake sequence, *Seismol. Res. Lett.,* **91(4),** 2055–2061.

Lomax, A., 2020. Absolute location of 2019 Ridgecrest seismicity reveals a shallow Mw 7.1 hypocenter, migrating and pulsing Mw 7.1 foreshocks, and duplex Mw 6.4 ruptures, *Bull. seism. Soc. Am.,* **110(4),** 1845–1858.

Luo, Y., Xia, J., Miller, R.D., Xu, Y., Liu, J. & Liu, Q., 2008. Rayleigh wave dispersive energy imaging using a high resolution linear Radon transform, *Pure appl. Geophys.,* **165,** 903.

Luo, Y., Xia, J., Miller, R.D., Xu, Y., Liu, J. & Liu, Q., 2009. Rayleigh wave mode separation by high resolution linear Radon transform, *Geophys. J. Int.,* **179,** 254–264.

Luo, Y., Yang, Y., Zhao, K., Xu, Y. & Xia, J., 2015. Unraveling overtone interferences in Love wave phase velocity measurements by Radon transform, *Geophys. J. Int.,* **203,** 327–333.

Masters, G., Woodhouse, J. & Gilbert, F., 2011. *Mineos v1.0.2 [software],* Computational Infrastructure for Geodynamics.

Matsuzawa, H. & Yoshizawa, K., 2019. Array-based analysis of multimode surface waves: application to phase speed measurements and modal waveform decomposition, *Geophys. J. Int.,* **218,** 295–312.

Nolet, G., 1975. High Rayleigh modes in western Europe, *Geophys. Res. Lett.,* **2,** 6–8.

Nolet, G., 1976. Higher modes and the determination of upper mantle structure, *PhD thesis,* Utrecht University.

Pedersen, H.A., 2006. Impacts of non-plane waves on two-station measurements of phase velocities, *Geophys. J. Int.,* **165,** 279–287.

Sergeev, S.N., Shurup, A.S., Godin, O.A., Vedenev, A.I., Goncharov, V.V., Mukhanov, Yu., Zabotin, N.A. & Brown, M.G., 2017. Separation of acoustic normal modes in the Florida Straits using noise interferometry, *Acoust. Phys.,* **63,** 76–85.

Tan, T.W., Godin, O.A., Brown, M.G. & Zabotin, N.A., 2019. Characterizing the seabed in the straits of Florida by using noise interferometry and time-warping, *J. acoust. Soc. Am.,* **146,** 2321–2334.

Trampert, J. & Woodhouse, J.H., 1995. Global phase velocity maps of Love and Rayleigh waves between 40 and 150 s, *Geophys. J. Int.,* **122,** 675–690.

van Heijst, H.J. & Woodhouse, J.H., 1997. Measuring surface-wave overtone phase velocities using a mode-branch stripping technique, *Geophys. J. Int.,* **131,** 209–230.

Visser, K., Trampert, J. & Kennett, B.L.N., 2007. Global Love wave overtone measurements, *Geophys. Res. Lett,* **34,** doi:10.1029/2006GL028671.

Wang, K., Dreger, D.S., Tinti, E., Burgmann, R. & Taira, T., 2020. Rupture process of the 2019 Ridgecrest, California Mw 6.4 foreshock and Mw 7.1 earthquake constrained by seismic and geodetic data, *Bull. seism. Soc. Am.,* **110**(4), 1603–1626.

Yoshizawa, K. & Ekström, G., 2010. Automated multimode phase speed measurements for high-resolution regional-scale tomography: application to North America, *Geophys. J. Int.,* **183,** 1538–1558.

Yoshizawa, K. & Kennett, B.L.N., 2002. Non-linear waveform inversion for surface waves with a neighborhood algorithm–application to multimode dispersion measurements, *Geophys. J. Int.,* **149,** 118–133.

Zeng, J., Chapman, N.R. & Bonnel, J., 2013. Inversion of seabed attenuation using time-warping of close-range data, *J. acoust. Soc. Am.,* **134,** EL394–EL399.

APPENDIX: A UNIFORM ASYMPTOTIC MODAL EXPANSION OF LOVE WAVES

We present here a normal mode expansion of Love waves excited by a point source in a stratified environment, making use of a uniform asymptotic treatment. eqs (A9, A12, A13, A16, A17 and A18) could be used as the basis for constructing Love wave synthetic seismograms for modes with turning depths far from the core–mantle boundary. The asymptotic dispersion relation, eq. (A16), plays a critical role in derivation of the warping transform. Although that equation is not new (see, e.g. Dahlen & Tromp 1998) the arguments presented here provide a relatively simple framework for generalizing that result as described later.

We use a cylindrical coordinate system: r is the horizontal distance from the source (assumed to be a point source); θ is the polar angle in the horizontal plane, so $\mathrm{d}y = r\mathrm{d}\theta$ is a small horizontal displacement normal to the radial direction; and z is the vertical coordinate, increasing upwards. v is the transverse horizontal component of ground motion velocity. Because we are interested only in very small ground motions at locations not close to the source (at $r = 0$) we may think of (r, y, z) as a local cartesian coordinate system and v as the y-component of ground motion velocity. We assume that medium properties, shear modulus μ and density ρ are functions of z only. In the following an overbar denotes Fourier transform, for example from $s(t)$ to $\bar{s}(\omega)$, with $\exp(-i\omega t)$ dependence assumed in the inverse Fourier transform. In the main body of this publication X (rather than r) is used to denote epicentral distance along a great circle path.

Assuming a conveniently normalized point source at $(r, z) = (0, z_0)$ with time dependence $s(t)$ the equation satisfied by $\bar{v}(r, z; \omega)$ is

$$\frac{1}{\mu(z)}\nabla\cdot(\mu(z)\nabla\bar{v}) + \frac{\omega^2\rho(z)}{\mu(z)}\bar{v} = -\frac{\bar{s}(\omega)}{\mu(z_0)}\frac{\delta(r)}{2\pi r}\delta(z - z_0). \tag{A1}$$

The upper surface is traction-free so $\partial\bar{v}/\partial z = 0$ at $z = 0$. Also, we assume that $\bar{v} \to 0$ as $z \to -\infty$. The homogeneous form of eq. (A1) admits a separable solution $\bar{v}(r, z) = R(r)\psi(z)$ (for convenience, ω-dependence is suppressed here). $R(r)$ and $\psi(z)$ satisfy

$$\frac{d^2R}{\mathrm{d}r^2} + \frac{1}{r}\frac{\mathrm{d}R}{\mathrm{d}r} + \omega^2 p^2 R = 0 \tag{A2}$$

and

$$\frac{d}{\mathrm{d}z}\left(\mu(z)\frac{d\psi}{\mathrm{d}z}\right) + \omega^2\rho(z)\psi = \omega^2 p^2\mu(z)\psi, \tag{A3}$$

respectively, where ω^2p^2 is a separation constant. The solution to eq. (A2) for $r \neq 0$ that satisfies the radiation condition at large r is a Hankel function of the first kind, $H_0^{(1)}(\omega pr)$. eq. (A3) together with the stated boundary conditions defines an eigenvalue–eigenvector (Sturm–Liouville) problem with weighting function $\mu(z)$. Solutions correspond to a discrete set of p-values (eigenvalues) p_n; eigenfunctions (normal modes) $\Psi_n(z; \omega)$ corresponding to different eigenvalues satisfy the orthogonality condition

$$\int_{-\infty}^{0}\mu(z)\Psi_n(z;\omega)\Psi_m(z;\omega)\,\mathrm{d}z = \delta_{nm}. \tag{A4}$$

Note that there is a different set of modes at each frequency and that it is assumed here and in the following that the modes are normalized. Completeness of the $\Psi_n(z; \omega)$ allows for a solution to eq. (A1) of the form

$$\bar{v}(z, r, ;\omega) = \sum_n A_n(\omega)\Psi_n(z;\omega)H_0^{(1)}(\omega p_n r), \tag{A5}$$

where the $A_n(\omega)$ are constants. The Hankel function satisfies

$$\left(\frac{d^2}{\mathrm{d}r^2} + \frac{1}{r}\frac{d}{\mathrm{d}r} + \omega^2 p_n^2\right)H_0^{(1)}(\omega p_n r) = 4i\frac{\delta(r)}{2\pi r}, \tag{A6}$$

so the $A_n(\omega)$ satisfy

$$\sum_n A_n(\omega)\Psi_n(z;\omega) = \frac{i}{4}\frac{\bar{s}(\omega)}{\mu(z_0)}\delta(z - z_0). \tag{A7}$$

By exploiting the orthogonality of the modes, eq. (A4), we find

$$A_m(\omega) = \frac{i}{4}\bar{s}(\omega)\Psi_m(z_0;\omega). \tag{A8}$$

Substituting $A_m(\omega)$ into eq. (A5) yields

$$\bar{v}(z, r, ;\omega) = \frac{i}{4}\bar{s}(\omega)\sum_n \Psi_n(z_0;\omega)\Psi_n(z;\omega)H_0^{(1)}(\omega p_n r). \tag{A9}$$

So far, the principal limiting assumption that we have made is the assumption that the environment is stratified. In addition, we note that evanescent energy is not accounted for in the modal sum, eq. (A9)

We turn our attention now to finding the p_n and the corresponding $\Psi_n(z; \omega)$. We make use of a uniform asymptotic treatment which, like traditional WKBJ methods, leads to good approximations to exact solutions when medium properties vary slowly on a scale of wavelengths. Additionally, the uniform treatment described here remains valid at modal turning depths where traditional WKBJ methods fail. Arguments similar to those presented here can be found, for example in Ahluwalia & Keller (1977). We assume that the horizontal shear wave speed $V = \sqrt{\mu/\rho}$ increases monotonically with increasing depth. (Our treatment does not account for energy trapped in low-velocity layers (LVLs). Because the Cartesian description used here is used after application of the Earth-flattening transformation this assumption is less restrictive than it might appear; a weak LVL in a spherical Earth model may be eliminated by the Earth flattening transformation. Also, even if an LVL is present, LVL-trapped modes are only very weakly excited by a source outside the LVL. For the purposes described in this paper, little is lost if the LVL is smoothed out, thereby eliminating LVL-trapped energy.)

The normal modes $\Psi_n(z; \omega)$ and corresponding p_n satisfy eq. (A3) with p replaced by p_n and $\psi(z)$ replaced by $\Psi_n(z; \omega)$. We retain for now the notation used in eq. (A3). Consistent with the stated assumptions we seek to find a solution of the form $\psi(z) = B(z)\,W[-\omega^{2/3}S(z)]$ where $W[x]$ satisfies the Airy differential equation $W''[x] - xW = 0$, while $S(z)$ and $B(z)$ are to be determined. Substituting $\psi(z)$ into eq. (A3), and subsequently collecting and equating terms on left and right in descending powers of ω, gives, to $O(\omega^2)$,

$$S(z)(S'(z))^2 = V^{-2}(z) - p^2, \tag{A10}$$

and, to $O(\omega)$,

$$B(z)\frac{d}{\mathrm{d}z}\left(\mu(z)S'(z)\right) + 2B'(z)\mu(z)S'(z) = 0. \tag{A11}$$

Let $\check{z}(p)$ denote the turning depth of the mode (or ray) whose horizontal slowness is p, where $V^{-2}(\check{z}(p)) = p^2$. Then the solution to eq. (A10) is

$$S(z) = \left[\frac{3}{2}\int_{\check{z}(p)}^{z}(V^{-2}(z') - p^2)^{1/2}\mathrm{d}z'\right]^{2/3} \tag{A12}$$

for $z > \check{z}(p)$ and

$$S(z) = -\left[\frac{3}{2}\int_{z}^{\check{z}(p)} (p^2 - V^{-2}(z'))^{1/2} \mathrm{d}z'\right]^{2/3} \tag{A13}$$

for $z < \check{z}(p)$. The solution to eq. (A11) is

$$B(z) = (\mu(z)S'(z))^{-1/2}. \tag{A14}$$

With $S(z)$ and $B(z)$ as defined here, the function W (recall $\psi(z) = B(z)\, W[-\omega^{2/3}S(z)]$) that satisfies the assumed lower boundary condition, $\psi \to 0$ as $z \to -\infty$ is the Airy function Ai. To satisfy the boundary condition $\psi'(z) = 0$ at $z = 0$ to leading order in ω, we make use of the large argument asymptotic relationship $\mathrm{Ai}'(-x) \sim x^{1/4}\pi^{-1/2}\sin((2/3)x^{3/2} - \pi/4)$. This leads to the condition

$$\sin\left(\omega\int_{\check{z}(p)}^{0} (V^{-2}(z') - p^2)^{1/2}\mathrm{d}z' - \frac{\pi}{4}\right) = 0. \tag{A15}$$

The integral in this expression is recognized as one-half the reduced traveltime $\tau(p)$, here based on the horizontal shear wave speed $V(z)$. To satisfy eq. (A15) the modal dispersion relation (or, equivalently, quantization condition)

$$\omega\tau(p_m) = 2\pi\left(\mathrm{m} + \frac{1}{4}\right) \qquad \mathrm{m} = 0, 1, 2, \ldots \tag{A16}$$

must be satisfied. At each frequency ω this equation defines a discrete set of p_m-values, which, in turn, are used in the corresponding functions $S_m(z)$ (eqs A12 and A13) and $B_m(z)$ (eq. A14). The final expression for $\Psi_m(z;\omega)$ is then

$$\Psi_m(z;\omega) = a_m(\mu(z)S_m'(z))^{-1/2}\mathrm{Ai}(-\omega^{2/3}S_m(z)), \tag{A17}$$

where a_m is a normalization constant which is constrained by eq. (A4). For $n = m$ this condition reduces to, after making a change of variables from z to $q_n(z) = \omega^{-2/3}S_n(z)$,

$$\omega^{-2/3}a_m^2\int_{-\infty}^{q_m(0)}\left(\frac{\mathrm{d}q_m}{\mathrm{d}z}\right)^{-2}\mathrm{Ai}^2(-q_m)\mathrm{d}q_m = 1. \tag{A18}$$

The normalization constant a_m is independent of the shear modulus profile $\mu(z)$, so, in the asymptotic treatment used here, the modal expansion of the wavefield (A9, A17) depends on μ only at the source depth z_0 and at the surface $z = 0$ where we seek to compute the ground motion.

The validity of the solution described above, including eq. (A16), is limited to modes with turning depths in the mantle far from the core–mantle boundary. That restriction can be relaxed by replacing the stretched depth dependence on Ai by dependence on a linear combination of Ai and Bi (the Airy function of the second kind) and applying a traction-free boundary condition at the core–mantle boundary. In the limit of small p_m (corresponding to steep reflecting modes) that solution leads to a dispersion relation similar to eq. (A16) but with 1/4 replaced by 0 (see also Dahlen & Tromp 1998). The same solution holds for intermediate (near grazing) modes, but in that case the dispersion relation is a more complicated expression involving the derivatives of Ai and Bi.